Multi-Layer Ultrasonic Imaging of As-Built Wire + Arc Additive Manufactured Components

Rastislav Zimermann, Ehsan Mohseni, David Lines, Randika K.W. Vithanage, Charles N. MacLeod, Stephen G. Pierce, Anthony Gachagan, Yashar Javadi, Stewart Williams, Jialou Ding

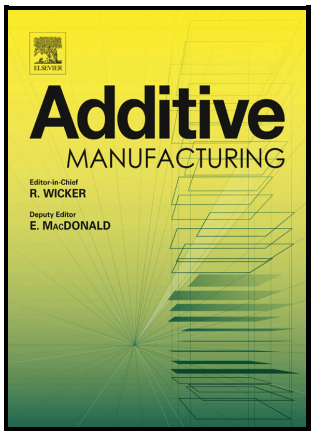

PII: S2214-8604(21)00551-0

DOI: https://doi.org/10.1016/j.addma.2021.102398

Reference: ADDMA102398

To appear in: *Additive Manufacturing*

Received date: 26 March 2021
Revised date: 28 September 2021
Accepted date: 8 October 2021

Please cite this article as: Rastislav Zimermann, Ehsan Mohseni, David Lines, Randika K.W. Vithanage, Charles N. MacLeod, Stephen G. Pierce, Anthony Gachagan, Yashar Javadi, Stewart Williams and Jialou Ding, Multi-Layer Ultrasonic Imaging of As-Built Wire + Arc Additive Manufactured Components, *Additive Manufacturing,* (2021) doi:https://doi.org/10.1016/j.addma.2021.102398

Additive Manufacturing, Volume 48, Part A, December 2021, Article number 102398
DOI:10.1016/j.addma.2021.102398

Multi-Layer Ultrasonic Imaging of As-Built Wire + Arc Additive Manufactured Components

Rastislav Zimermann[1], Ehsan Mohseni[1], David Lines[1], Randika K. W. Vithanage[1], Charles N. MacLeod[1], Stephen G. Pierce[1], Anthony Gachagan[1], Yashar Javadi[1], Stewart Williams[2], Jialou Ding[2]

[1]Centre for Ultrasonic Engineering, University of Strathclyde, Glasgow, UK
[2] Welding Engineering and Laser Processing Centre, University of Cranfield, Cranfield, UK

Corresponding Author: Rastislav Zimermann, rastislav.zimermann@strath.ac.uk,
Centre for Ultrasonic Engineering, Department of Electronic & Electrical Engineering, University of Strathclyde, 204 George Street, Glasgow, G1 1XW, United Kingdom

Abstract

Non-Destructive Evaluation (NDE) of metal Additively Manufactured (AM) components is crucial for the identification of any potential defects. Ultrasonic testing is recognised for its volumetric imaging capability in metallic components and high defect sensitivity. However, conventional ultrasonic techniques suffer from challenges when deployed on components with curved and non-planar geometries, such as those often encountered in AM builds.

The body of work introduces the concept of inspection of Wire+Arc Additive Manufacture (WAAM) components from their non-planar as-built surface, eliminating the requirement for post-manufacturing machining. In-situ or post-manufacturing inspection is enabled via an autonomously deployed conformable phased array roller-probe deploying Synthetic Aperture Focusing Technique (SAFT)-surface finding and multi-layer adaptive Total Focusing Method (TFM) algorithms, for fully focussed imaging of the as-built WAAM component.

The concept of the imaging approach is demonstrated by inspection, through the as-built surface, of two titanium WAAM components, one containing reference bottom-drilled holes, and the other with intentionally introduced Lack of Fusion (LoF) defects.

The TFM images of the WAAM components feature sufficient Signal-to-Noise Ratio to enable defect detection along with strong agreement against reference X-Ray CT data, confirming the competency of the approach for volumetric or layer-specific inspection of as-built WAAM components.

Keywords:

Ultrasound inspection of additive manufacturing, ultrasound array imaging, Adaptive Total Focusing Method (ATFM), Full Matrix Capture (FMC), Synthetic Aperture Focusing Technique (SAFT), Wire + Arc Additive Manufacture (WAAM),

1. Introduction

1.1: Additive Manufacturing

Additive Manufacturing (AM) is a process of joining materials layer upon layer to produce components from 3D model data [1]. AM is a substitute for traditional manufacturing methods, in which, the components are commonly subtracted by milling processes or formed in molds [2]. In AM of metals, a powder or wire feedstock is melted by an energy source. Powder bed fusion processes such as laser beam melting, or electron beam melting are used to build components in closed chambers by fusing the powder to create a layer of the final structure. The bed on which the layer is deposited is then lowered and the process is repeated until the full component is completed. The key advantage of such a process is the high geometric accuracy of the final component however, the process is traditionally slow; hence, the components produced are typically small [3]. Large scale application of additive manufacturing is commonly associated with directed energy deposition processes, such as laser metal deposition or Wire+Arc Additive Manufacturing (WAAM), where a wire or powder is fed into the melt pool created by laser, electron beam or an electric arc. The dimensional accuracy of these processes is commonly traded against the increased size of the final component and the deposition speed [2].

1.2: Wire + Arc Additive Manufacturing (WAAM)

Industrial sectors such as aerospace, defence and energy have shown a growing interest in the capability of WAAM, as the process offers the potential for manufacturing cost-effectiveness owing to reduced material waste, decreased production time and increased design flexibility when producing large and complex components as shown on Figure 1 (a) [4]. For instance, the authors have reported material savings of approximately 220 kg in manufacturing of a 24 kg titanium Ti-6AL-4V (Ti-64) landing gear assembly with a deposition rate of 0.8kg/hour. [4]. In this example, the component consisted of complex features such as tiled walls and T-junctions, proving the process as a suitable replacement for traditional subtractive techniques where machining and waste make the process inefficient. [5]. The titanium alloy utilized is extensively used in aerospace and chemical engineering because of its good fracture toughness, high strength and corrosion resistance. [6].

WAAM components are typically deposited robotically using an electric arc, acting as a heat source, along with wire feedstock in a similar fashion to welding, as illustrated in Figure 1(b) [4, 7]. The component geometry is commonly a series of deposited walls with parallel or single oscillating beads. [8]. When depositing materials that could suffer from oxidation and subsequently have induced defects during deposition, additional shielding is required. In [8], WAAM deposition of large titanium components was enabled through the deployment of a local shielding device (Fig 1 (b)) which supplies the build area with shielding gas, such as argon or helium and reducing the potential for contamination. Additional methods of shielding WAAM deposition utilize tent-like structures, fully enclosing the deposition apparatus and filled with shielding gas to reduce the components contact with oxygen to a minimum. [9].

Although the shielding system protects the molten pool from oxidation, reducing the potential for porosity and inclusions, similar to many welding or manufacturing processes, Lack of Fusion (LoF) and keyholes defects may occur in the components affecting their structural integrity and fitness for service. [10]. These undesired deposition defects in safety-critical WAAM components predominantly originate from the poor quality of the wire, incorrect definition of the process parameters and contamination introduced by the environment. [4]. Therefore, it is essential to assess the quality and integrity of manufactured components through Non-Destructive Evaluation (NDE) before they can be certified and enter their intended service application.

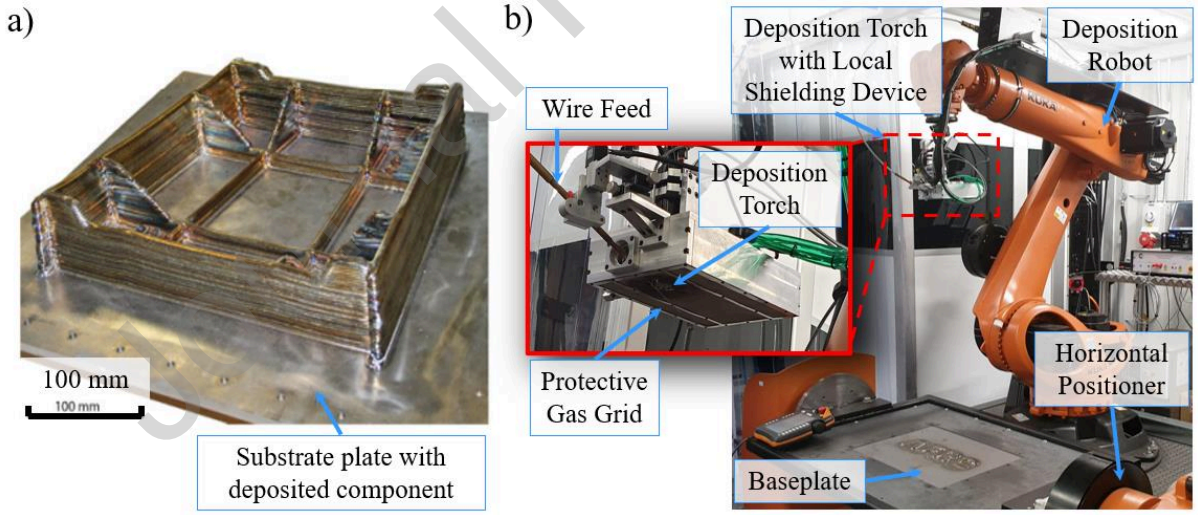

Figure 1 (a) WAAM landing gear rib component, and (b) WAAM robotic deposition setup [4]

1.3: Inspection of Additive Manufactured Components

NDE is a process for evaluating the structural integrity and characteristics of a component without affecting the useful serviceability of the part.

X-ray imaging techniques such as radiography have already been successfully utilized and evaluated on AM components, detecting porosity, inclusions and lack of fusion defects in fully-built WAAM components [11]. In X-ray testing, radiation energy is sent through the component and captured by an analog or digital photosensitive reception medium to form an image showing inconsistencies of the penetrated energy caused by volumetric discontinuities. However, the application of this technique is generally time taking, hazardous and expensive [12].

More advanced techniques such as X-ray Computed Tomography (XCT), have also been utilized on AM components. In XCT, normally a series of X-ray images are taken from different angles surrounding an object, and then, the 3D model of the component is constructed via computing the amount of X-ray exposure of constituent cubic elements of the 3D volume [13]. The technique shows sensitivity to detect and characterize defects deep within AM components, without the need for surface preparation and has been demonstrated of detecting defects as small as 600μm in titanium components produced using electron beam techniques [14]. The downside of this technique is, however, the costs associated with the equipment and analysis station, and the impracticality of in-situ inspection of large components [15].

Regarding the application of electromagnetic-based inspection techniques, Eddy Current Testing (ECT) is a technique where circular currents are generated in a conductive material by a coil connected to a current generator and where a defect is highlighted by perturbations in the current [16]. ECT with customized spatially design coils, with a shape matched to the as-built curved surface of a WAAM component, were shown to be capable of detecting side-drilled holes of 0.35 mm at depths of 2 mm in aluminum samples [17]. Even though ECT offers very high surface/near-surface sensitivity and detectability, the penetration depth is traditionally limited to a few millimeters below the surface depending on the coil design, test frequency, and material properties [16]. Therefore, while it offers the potential for on-line screening of newly deposited upper layers during the manufacturing process [11], it is not best-suited for deeper volumetric inspection of WAAM components and multi-layers, or the in-process inspection of preceding layers for defects such as delayed cracking [18, 19].

Among other NDE methods deployed for the AM inspection, thermography has also shown promise when used within the deposition cell and with a safe distance from the heat source to monitor the defect formation during the process allowing for possible in-situ repair [14]. During the thermography tests, the variations of the thermal gradient indicating the flaws were monitored in the AM components. The downside of this technique is, however, the lower sensitivity in-depth and due to surface roughness alongside the time required to induce the required heat in the sample [20].

Conventional Ultrasound Testing (UT) or modern phased array technology is often the preferred inspection technique for volumetric examination of metallic welded components [21]. This inspection method offers high sensitivity to small defects and is capable of pinpointing, characterizing and sizing different shapes and orientations [22]. Additionally, considering the advances in phased array technology, signal processing and robotics, the technique is feasible to integrate within automated robotic systems for the inspection of welds and AM components efficiently and safely [23, 24]. Typically, in weld inspection, angled wedges mounted alongside the joint on the parent material, are normally required to guide the wave towards the weld at a certain defined angle or the emerging use of novel conformable liquid-filled delay lines allow inspection directly on top of the fully filled weld cap [24].

Laser ultrasound, as another mechanical method of generating ultrasonic waves, is a non-contact method capable of detecting defects as small as 0.2mm in diameter in AM components and has shown potential for on-line monitoring [25]. The method has been deployed to detect subsurface defects of AM components produced using laser powder bed fusion [25] and on WAAM components detecting surface cracks, flat bottom holes and through holes [26]. However, laser ultrasonic setups have historically featured very high initial costs, slow generation, acquisition and data processing times, while also being sensitive to surface finish [27] and safety considerations.

Lastly, the deployment of gas or air-coupled UT is inherently limited by the large acoustic impedance mismatch between the air and solid inspection medium, resulting in a large loss of energy (< 140 dB) and hence sensitivity, therefore not endearing this method for the inspection of AM components [28].

Considering the capabilities of NDE techniques previously trialed on AM components and summarized above, ultrasonic techniques offer strong potential for in-situ as-built WAAM volumetric inspection. However, challenges remain related to suitable coupling between the ultrasound probe and the as-built WAAM surface, along with imaging of the component through the irregular as-built surface.

1.4: In-Situ Inspection of As-Built WAAM Components

Traditionally, WAAM component manufacturing and NDE tend to be conducted separately and sequentially within the build process. Merging both these processes by incorporating the NDE within the manufacturing cell aims to save time and costs associated with part relocation and transfer between the cells [24]. In current ultrasonic inspection practices, completed AM components are either: (a) scanned inside immersion tanks using

gantry systems, or (b) manually tested after their surface is machined flat for contact ultrasonic inspection [29-32] [33, 34]. However, immersion testing of large-scale WAAM components is very challenging and sometimes impractical, and even in such a configuration, a flat machined surface is preferred to avoid the ultrasonic wave refracting and scattering at the surface/couplant interface. Moreover, to conduct the immersion test, the component is often transferred to another cell prolonging the full build process significantly.

For conventional ultrasonic testing to be performed on a WAAM component, often a milling operation must be introduced into the production cycle [35], again to avoid wave refraction and scattering at the surface/couplant interface. Such surface machining increases the component processing time and cost, while delaying the inspection and lowering the throughput. In [29], the components were inspected by a UT probe from below the bottom base plate [29] and although this method eliminates the need for top surface machining, it is not a viable option for the increasingly common components which utilize double-sided deposition strategies to minimize residual stresses and prevent component distortion [36]. Furthermore, a manual ultrasonic inspection of large scale WAAM components is very time-consuming creating further bottlenecks in production. Additionally, traditional ultrasonics probes are typically only functional up to 60 °C, and with the WAAM as-built surface potentially being at hundreds of degrees Celsius just after the deposition [37] further cooling times and delays are required to be introduced into the inspection process.

The acoustic coupling in ultrasonic inspections is usually established through an acoustic liquid gel, where a thin layer removes any air gaps between the transducer and the surface due to material roughness or geometrical unevenness; thus, allowing transmission of the ultrasound wave into the component. Such a liquid gel is however not ideally suitable for in-situ inspection of WAAM components since it would require a constant supply delivered to the probe and WAAM surface, likely contaminating the build if a further deposition is required. Despite emerging water wedges [38] that are capable of conforming to the rough upper surface of WAAM components, still require an acoustic gel to ensure coupling and allow movement and reduce wear of the probe surface.

Non-contact ultrasound inspection techniques such as Laser Induced Phased Arrays (LIPA) [6] and air-coupled UT could bypass these surface coupling challenges, and while LIPA has shown great potential for detecting small defects in AM components, among its main shortcomings is the need for smooth polished surfaces [39] inconsistent with the as-built WAAM surface.

Contact techniques, that allow transmission of ultrasonic energy into a specimen without the use of liquid couplants, offer the potential for dry-coupling and reduced surface contamination. Such dry-coupling can be provided by acoustically matched polymers, which feature low attenuation and wave velocities similar to water [40] and [41]. When placed between the transducer and the sample and suitable force is applied, the air between the two mating surfaces is expelled and the acoustic energy is transferred. However, when considering automated deployment and surface scanning, excessive and damaging shear forces can be introduced from dragging these polymers across the surface resulting in increased wear and reduced life. A dry-coupled phased array probe, specifically designed for automated in-process inspection of welds was introduced in [42], which can resist elevated temperatures and enable rolling motion across surfaces.

This body of work presents for the first time an ultrasonic phased array volumetric imaging concept that can be deployed on the as-built surfaces of WAAM components. Firstly, a dry-coupled contact-based, high-temperature compliant phased array ultrasound roller-probe for WAAM inspection is introduced. Furthermore, the concept and development behind a three-layer adaptive TFM imaging algorithm is introduced and explained. Finally, the resultant non-destructive imaging of two titanium WAAM components, with artificial and process defects was explored and characterized against XCT with a successful correlation between both techniques.

2. Dry-Coupled in-situ Ultrasonic Inspection of as-built WAAM Components

2.1: Automated As-Built WAAM Component Inspection

When considering the design and the implementation of an ultrasound probe for in-situ deployment on as-built WAAM components, two main challenges emerge: (1) Acoustic coupling of the sound into the component through the as-built surface, and (2) Withstanding the elevated surface temperatures of the as-built component.

These challenges can be overcome by using a dry-coupled ultrasonic roller-probe. Conventionally, a roller-probe is a device with either a single element or a phased array transducer mounted within an acoustically friendly rubber wheel allowing for faster manual inspection of larger components [41, 43]. Subsequently, the roller-probe technology has been adapted to the needs for automated inspection of large structures [44, 45]. The recent development has also shown a deployment of the high-temperature liquid-filled roller-probe on in-process inspection of multi-pass welds [42]. In this work, a roller-probe is designed for the dry-coupled inspection of large scale WAAM components in order of centimetres/meters [46] but has the potential to be adapted to a variety of large scale additive manufacturing techniques or large structures. The WAAM roller-probe, illustrated in Figure 2, is equipped with a watertight rotary rubber tire and a delay-line, through which the ultrasonic wave generated by the ultrasonic array can propagate. A solid delay line enables conformance of the rubber to the surface of WAAM by a sufficient amount of force. The ultrasonic array is mounted in the center of the roller-probe on the delay line. A key advantage of this design can be realized in automated inspection setups, where the rotary design directly facilitates automated delivery and smooth manipulation over varying profile surfaces at speed. Additionally, the roller-probe is designed to withstand surface temperatures of up to 350°C, meaning it can be deployed on the WAAM surface just after deposition when the sample is still at elevated temperatures, either in-situ or after the full built is completed.

The WAAM roller-probe is designed to accommodate the mismatch between the flat surface of the delay-line, inside the roller-probe, and the as-built WAAM surface profile and curvature using the high-temperature compliant flexible rubber tire. Accordingly, the ultrasound waves generated by the array propagates through three mediums: 1) the delay line medium, 2) the rubber tire and 3) the WAAM component, as depicted in Figure 2. The ultrasonic beam refracts at two interfaces namely the delay line/tire and tire/WAAM boundaries with the latter being a curved interface. Refraction due to any acoustic velocity mismatch between the materials changes the direction of the beam as it propagates through the layers [47, 48]. Therefore, to compute the precise volumetric image of the WAAM component, the challenge of ultrasound wave propagation and refraction through three layers must be addressed.

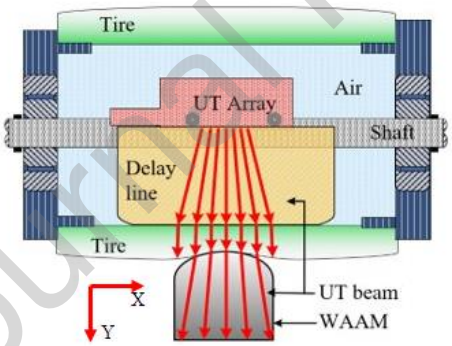

Material	Acoustic Velocity (m/s)
Delay line	2480
Tire	1006
WAAM	5800 - 6300

Figure 2 A schematic of the high-temperature roller-probe in contact with a WAAM sample

2.2: Automated As-Built WAAM Component Imaging

Ultrasonic imaging and beam tracing through three refractive layers with arbitrary interfaces is difficult to overcome using conventional ultrasonic methods such as electronic beamforming [49]. In beamforming imaging, the phased array delay laws are calculated prior to the scan to focus the beam at a specific depth through knowledge of the material interfaces and then the array is excited using the focal laws to form a B-scan image with fixed limited resolution. However, as soon as the curvature of the interface changes during the scan, in this case, the WAAM as-built surface, the focal laws require to be recalculated for an optimal beam focus and Signal-to-Noise Ratio (SNR). This process requires the continuous online acquisition of the surface profile to constantly update the focal laws, greatly affecting scan speed and rendering such methods inefficient for automated applications where high scanning speeds are desired. In view of these, alternative fully focused imaging processes that can accommodate high scan speeds should be sought for automated inspection applications.

Such an objective can be attained through a combination of real-time data acquisition and processing. Full Matrix Capture (FMC) is a process where the signal from a full combination of all transmitting and receiving

combinations are acquired is proposed for future automated inspections. The complete set of time-domain data acquired through FMC allows for the implementation of a wide range of post-processing algorithms that seek to address all the challenges presented [48].

The collected FMC data can then be used to form images using post-processing algorithms, such as the Total Focusing Method (TFM), based on Delay-And-Sum (DAS) computational logic, and enabling superior resolution and sensitivity to smaller defects when compared to conventional beamforming inspections [50]. The technique calculates the Time of Flights (ToF), also called the delays, between each array element and every pixel of the image. Based on these delays, the signal amplitudes from the individual A-scans are summed in the final image. [50].

When considering multiple media inspection, current TFM inspection methods, however, have been mainly developed for the two-media inspection of components from either ultrasonic delay-lines placed on the flat surfaces, or wedges on weld plates [51]. When it comes to ultrasonic imaging of components with complex geometries, the main research focus has been placed on two-media adaptive TFM imaging for immersion (water/sample) setups or water-filled conformable delay lines used in contact with complex surfaces [52]. Such two-media algorithms are application-specific and are not fit for the purpose when considering the three-media inspection of as-built WAAM components using the roller-probe introduced above.

Therefore, a modified adaptive TFM algorithm is proposed herein to account for the three mediums (delay-line, tire and WAAM component) and the two interfaces with compensation for the as-built WAAM surface curvature. The performance of the algorithm is then assessed through imaging and inspection of as-built Ti-64 WAAM components with both Bottom-drilled Holes (BH) and intentional LoF defects. The LoF defects were also scanned using micro-focus XCT to verify and compare the results of the adaptive TFM algorithm.

2.3: Ultrasonic Imaging through Arbitrary Unknown Surfaces

To be able to form TFM images of the WAAM components after FMC acquisition, the geometry of the unknown interfaces should be identified. Given the known and flat delay-line/tire interface, it is only necessary to include a stage to reconstruct the tire/WAAM interface surface profile. The surface finding algorithm developed for this work is based on a dual-medium Synthetic Aperture Focusing Technique (SAFT) imaging.

Utilizing SAFT instead of TFM for the surface imaging was studied in [53], where TFM was not able to present a full contour of the tested specimen due to the high-intensity side lobes, while SAFT presented a clean contour without disruption by false signals.

Like TFM, the SAFT imaging is a DAS post-processing algorithm that employs a sub-aperture of elements for constructing an image. In the SAFT algorithm, the contribution of elements to the image pixels is predetermined by the angle intervals. Once the image is computed, a surface profile is extracted autonomously by isolating the pixels with the signal intensity above a threshold and fitting a curve. Achieving a high precision surface profile is an important step in this work as even minor profile errors could result in loss of image quality due to loss of focus coherence in the final TFM imaging stage [54].

In this paper, for the first time, a novel hybrid SAFT and TFM algorithm was developed to identify the unknown as-built WAAM surface and compute a TFM image of the cross-sectional WAAM wall while inspecting through 3-layers. Contact ultrasound inspection and FMC data collection were made possible owing to the innovative high-temperature phased array roller-probe design that is conformable to the as-built surface of the WAAM components. The hybrid SAFT + TFM algorithm together with the roller-probe were combined to form a unified inspection methodology for automated high-speed inspection and imaging of WAAM components.

3. Ultrasonic Imaging through Three-layers and Arbitrary Complex Surfaces

3.1 The Full Matrix Capture (FMC) and Total Focusing Method (TFM)

Ultrasonic arrays were used for the data acquisition process, where time-domain signals from every pair of the transmit (Tx) -receive (Rx) elements were collected to form the FMC dataset. For a linear array with *N* elements, a total number N^2 A-scans were recorded. The illustrations of Figure 3(a) show the sequence of transmit-receive elements activated in an FMC acquisition mode where a single transmit element was stepped by 1 between 1 to *N*, and for each transmission, all the *N* elements were used in the reception.

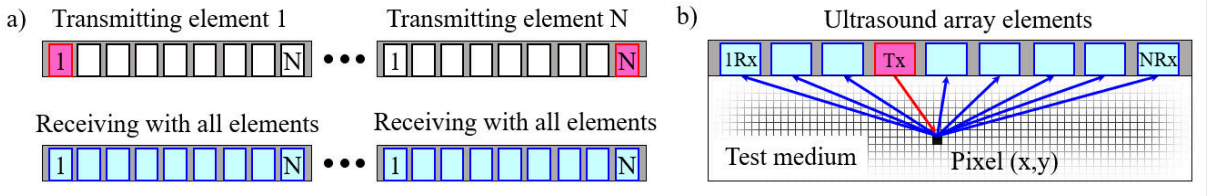

Figure 3 Diagram explaining (a) full matrix capture data collection, and (b) total focusing method

The FMC dataset served as the input to the TFM images that were subsequently processed using a DAS algorithm. In the TFM algorithm presented here, the full aperture of the array was used to synthesize a focus on every pixel of the image at both the transmission and the reception stages, as shown in Figure 3(b), allowing higher resolution across the whole image, and therefore, a higher sensitivity to smaller defects. For every image pixel *P* within the inspection medium, the image pixel intensity *I(P)* for each transmit-receive *(k, l)* combination was calculated through:

$$I(P) = \sum_{k=1}^{N}\sum_{l=1}^{N} S_{k,l}\left(T_{Tx(k)} + T_{Rx(l)}\right) \quad (1)$$

where, $S_{k,l}$ is the time-trace associated with the A-scan of every Tx-Rx combination, $T_{Tx(k)}$ represents a ToF from the transmitted element to the pixel P, and $T_{Rx(l)}$ stands for the return journey from the pixel P to the element. A TFM image frame ($I_{(i,j)}$), with grid point indexes *(i, j)*, was computed using the elementary A-scans within the FMC dataset, while a secondary one ($I'_{(i,j)}$) was also obtained through a Hilbert transform of the A-scans with the application of the same delays. Consequently, the TFM envelope ($I_{envelope}$) was calculated using the following formula:

$$\left|I_{envelope}\right| = \sqrt{(I_{(i,j)})^2 + (I'_{(i,j)})^2} \quad (2)$$

Therefore, the resulting image was composed of two TFM images: (I) one produced from the real component of the elementary A-scans, and (II) the other from the imaginary component of the elementary A-scans. The main advantage of the enveloped image lies in the possibility of increasing the grid pixel size, and hence, curtailing the computation time needed to compute the image without losing the intensity of the signal [55]. Finally, to present the pixels in a dB scale with the reference to the maximum amplitude of the image, the pixel amplitude I_{amp} values were normalized by the maximum amplitude I_{amp_max} present in the image as shown in Equation 3.

$$I_{amp\_norm} = 20 \times log_{10}\left(\frac{I_{amp}}{I_{amp\_max}}\right) \quad (3)$$

3.2. Focusing Through Multiple Media

This body of work aims to implement TFM imaging of WAAM components through three mediums and across two interfaces. These are the fixed planar delay-line/tire interface inside the PAUT probe and the non-planar tire/WAAM arbitrary contour interface on the as-built WAAM surface. The delay calculations were carried out according to the minimum ToF principle, which is also known as Fermat's principle [56]. In the case of homogeneous media, a straight line connecting an element and an image pixel best describes the path along which an ultrasonic wave generated by the element traverses to reach a specific image pixel. However, when a media constituted of multi-materials with different acoustic properties is considered, the ultrasonic waves generated by the elements refract across the interfaces before reaching the image pixel in the target medium; hence, the orientation of the wave travelling path varies in each medium. To this end, the ToF's should be calculated individually in each medium as illustrated in Figure 4. In the cartesian coordinates, the algorithm for ToF $T_{(Tx,Rx)}$ for both Tx and Rx array elements to pixel P (*x, y*) in the WAAM component can be formulated as:

$$T_{(Tx,Rx)} = \frac{\sqrt{(x_{i1} - x_t)^2 + (y_{i1} - y_t)^2}}{v_1} + \frac{\sqrt{(x_{i2} - x_{i1})^2 + (y_{i2} - y_{i1})^2}}{v_2} + \frac{\sqrt{\left(x_p - x_{i2}\right)^2 + \left(y_p - y_{i2}\right)^2}}{v_3} \quad (4)$$

where the $(x_t\ ,\ y_t)$, the $(x_{i1}\ ,\ y_{i1})$, the $(x_{i2}\ ,\ y_{i2})$, and $(x_p\ ,\ y_p)$ are respectively, the coordinates of the array elements, the incidence point of the ultrasound ray to the first interface, the incidence point of the ultrasound ray to the second interface, and the targeted pixel. The (v_1), (v_2) and (v_3) are the velocities in the first, second and third medium.

The wave refraction angles at the interfaces were also calculated using Snell's law which is presented in its most common form in Equation 5, where θ_i and θ_r represent the angles of the incidence and the refraction, respectively, as illustrated in Figure 4(a). It should be noted that the refraction angle at the incidence point on the arbitrary profile was also calculated with respect to the normal of the surface at the point illustrated in Figure 4.

$$\frac{Sin(\theta_i)}{v_1} = \frac{Sin(\theta_r)}{v_2} \quad (5)$$

In this work, a root-finding algorithm based on a bisection method was developed and used to trace the ultrasound ray path between the array elements and the image pixels to a precision defined by the user. Clearly, higher precision demands a longer algorithm runtime due to the increased number of iterations required to converge to a solution. The ray-tracing workflow used within the algorithm is shown in Figure 5(b) and demonstrated in Figure 4(b), and can be summarized in the following steps:

1. At the first interface (delay-line/tire), evenly distanced finite number of nodes (i'_n) are initially generated.
2. The ray (Tx_n), with *(n=Node number on the first interface),* transmitted from an element is connected to each of the nodes with the straight lines and the refracted angles calculated at the first interface and at each node.
3. The point coordinates at which the rays refracted from the first interface impinge the second interface are found, and the resulting refraction angles from the second interface are obtained.
4. The $T_0,\ldots,T_n$ points where the rays refracted from the second interface $(i2)$ approach the pixel's *y* coordinate are indicated and the positional error of the rays in the *x*-direction with the reference to the target pixel assessed. Subsequently, the two coordinates closest to the pixel of the pixel are selected while the rest of them are discarded.
5. If the error is larger than the maximum allowed distance between an incoming ray and the pixel point, a new i' is selected. Otherwise, the path with the lower error is stored and a new pixel-element pair calculated.
6. To select a new i'_n, the error coefficient (c) is obtained as an absolute value of the division of the two errors between T_0 , T_1 and targeted pixel. It is necessary to make sure that $0 \leq c \leq 1$, thus a larger error is always divided by a smaller value.
7. The coefficients are then applied, where the distance between two previously used i'_n and i'_{n-1} are subtracted and multiplied by the coefficient, giving a new offset. Subsequently, this offset is added or subtracted from the latest i'_n depending on whether the T_n is larger or smaller than a targeted pixel.
8. The process is iterated until the distance measured between the T_n and the pixel becomes smaller than the error indicated. This yields the ray path (Tx) and the ToF from an element to a pixel in the image.
9. The process is repeated until the ToF's for all the combinations of elements and pixels is reached.

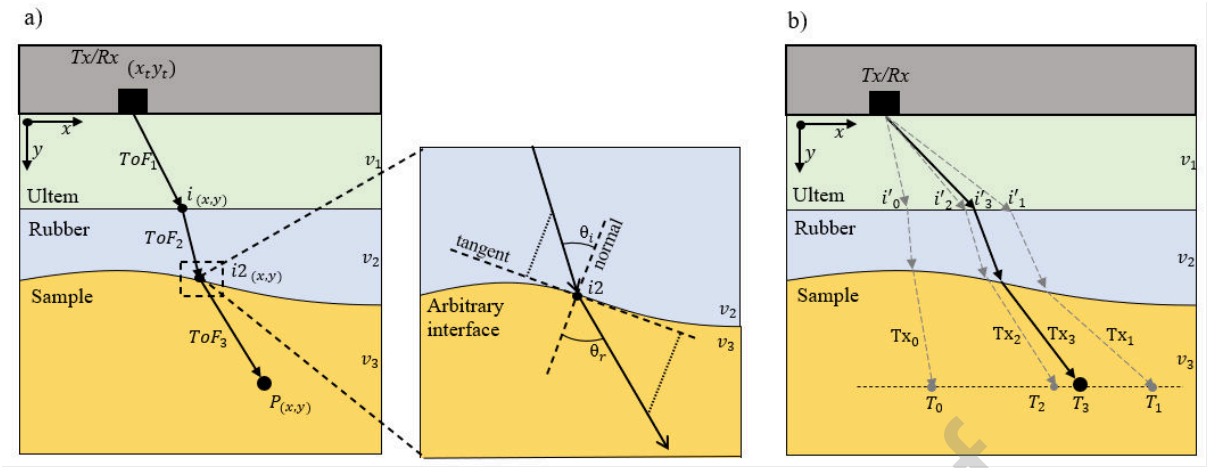

Figure 4 Schematic diagram showing a) ray tracing and time of flight calculations between an array element and a target pixel through three media with refractions on planar (delay-line/tire) and non-planar (tire/WAAM) interfaces, and b) iterative process and convergence to a target pixel using the search algorithm.

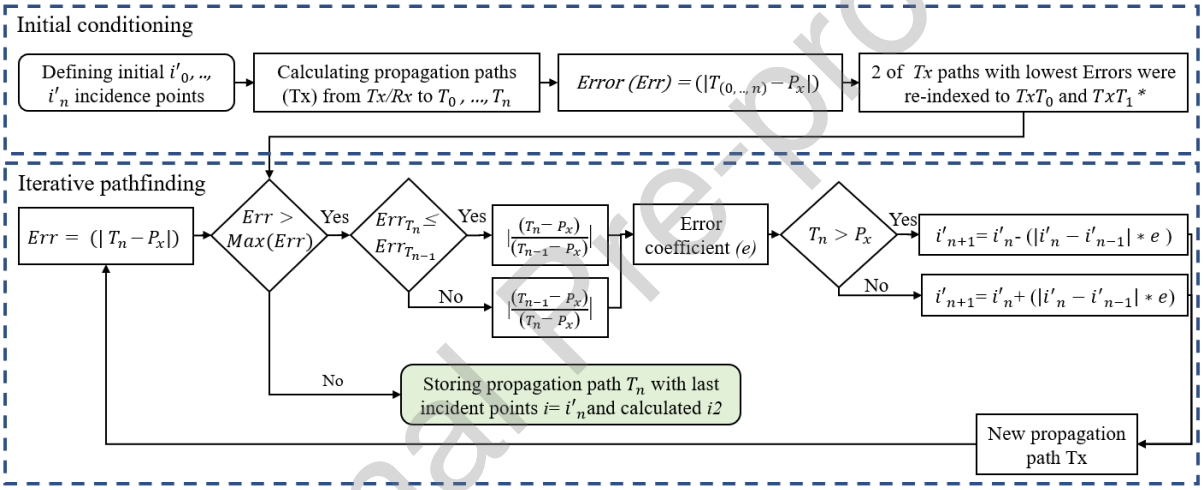

Figure 5 Diagram explaining the search algorithm developed for ultrasonic ray-tracing

3.3.1 Ultrasonic Driven WAAM Surface Reconstruction

The first step taken in the imaging process is to estimate the surface profile of the WAAM component. Knowing the planar interface (delay line/tire), the WAAM interface region can then be imaged directly. For this purpose, a dual-medium (*i.e.* propagation through the delay-line towards the bottom of the tire) DAS SAFT algorithm with angular aperture limit was developed. The limitation is defined by α and β marking the angles between the outmost rays focused at each pixel and the normal of the first interface, as depicted in Figure 6. The intensity of each pixel P in the image was computed using the velocity of the first (v_1) and second (v_2) media only, and given by:

$$I_{rubber}(P) = \sum_{k=1}^{N} \sum_{l=\alpha}^{\beta} S_{k,l} \left(T_{Tx(k)} + T_{Rx(l)}\right) \tag{6}$$

Where, $T_{(Tx,Rx)}$ was calculated in coordinate system (x, y) and was given by:

$$T_{(Tx,Rx)} = \frac{\sqrt{(x_1 - x_t)^2 + (y_{i1} - y_t)^2}}{v_1} + \frac{\sqrt{(x_{i2} - x_{i1})^2 + (y_{i2} - y_{i1})^2}}{v_2} \tag{7}$$

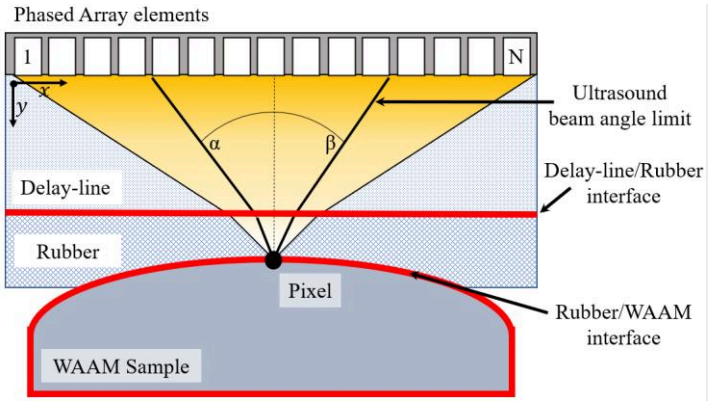

Figure 6 Diagram illustrating the phased array elements contribution to the pixel of the SAFT image targeting the tire/WAAM interface, and limited by the angles α and β

3.3.2 Ultrasonic Driven WAAM Surface Profile Extraction

Once the surface image is generated, global thresholding is used to extract the surface points. The algorithm is designed for automated surface reconstruction sweeps of the image, column by column, to identify the pixels with the highest intensity value above the defined threshold. If two identical values coexist in the same column, the algorithm retains the pixel with the lower *y* coordinate in Figure 10 (c). This is introduced to prevent the occurrence of errors due to stronger signals received from the inside of the specimen or attributed to the second reflection. Knowing the characteristic surface finish of WAAM builds deposited with common deposition strategies, which typically represent a semi-elliptical shape with waviness, the extracted pixels were sufficiently defined with a 4^{th} order polynomial curve, smoothed by the local polynomial regression also known as moving regression. Smoothing of the curve was necessary to avoid potential distortions of the curve caused by dislocated surface points wherever a false echo is present in the surface image.

4 Experimental Setup

4.1 Phased Array Ultrasonic Inspection Configuration

The ultrasonic roller-probe used in the experiments encompassed a 5 MHz 64 element linear array with specifications presented in Table 1.

Table 1 phased array probe parameters

Array Parameters	Value
Element Count	64
Element Pitch	0.5 mm
Element Elevation	10 mm
Element Spacing	0.1 mm
Centre Frequency	5 MHz

The array transducer was mounted on a 26 mm high delay-line with a density of 1.27 g/cm³ and an acoustic velocity of 2480 ms^{-1} inside the roller-probe. A liquid gel was used as the couplant at the interfaces of the array/delay-line and the delay-line/tire. A 6 mm thick, soft silicone rubber tire, with high-temperature compliance (350 °C) constituted the exterior layer of the roller-probe [57]. Figure 7 demonstrates the experimental setup where the roller-probe was mounted on a 7-axis KUKA LBR robotic arm that featured embedded force-torque sensors in its joints. The robot provides the force-torque values of the end effector, and this feature was used to ensure a constant contact force of 50 N between the roller-probe and the WAAM component. FMC data was collected at 12-bit resolution using a Peak NDT LTPA phased array controller with 200 V excitation voltage and fixed hardware gain of 65 dB. The time-domain matrix of the signals was formed by 8000 data samples for each transmit-receive pair A-scan at a sampling frequency of 50 MHz.

The SAFT surface identification and TFM imaging algorithms were integrated and implemented in MATLAB 2020a. The processing time was evaluated on an AMD Ryzen Threadripper 3960 24 core Processor

with a clock speed of 3.79 GHz and 128 6Gb of Random-Access Memory. The elapsed time for the SAFT algorithm to estimate the surface contour was 3.1 seconds, and the convergence for the ray tracing and the TFM image creation was 30 seconds. Although in this work the speed of the algorithm was not the prime importance and was not optimized, further modifications will be investigated to leverage the computing power of Graphics Processing Units (GPU) and to minimize this computation time. Optimizing for GPU usage can offer the advantage of splitting the execution on a much higher number of cores compared to a low number of CPU cores.

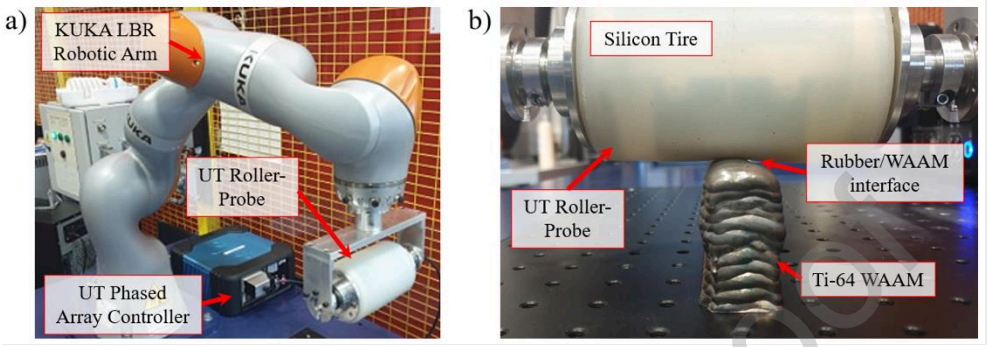

Figure 7 Robotic ultrasonic inspection set-up consisting of (a) a KUKA robotic arm, ultrasound phased array controller, and (b) an ultrasonic roller-probe placed on a titanium WAAM sample

4.2 Process Flow of In-Situ Imaging of As-Built WAAM Components

Figure 8 shows the imaging process flow where the images for a surface finding algorithm were built to have 10 pixels per image millimeter of the image generating a grid of 320×60 pixels. The height of the imaging window was selected as 5 mm, to enclose the entire span of the tire/WAAM interface, where the surface profile was expected to lie. The final adaptive TFM images were computed using 5 pixels per image millimeter, thus the verification sample was imaged using a grid of 160×75 pixels and the defective titanium wall imaged using 100×50 pixels, optimized from coarser larger areas scans.

The SAFT surface images were processed assuming constant longitudinal wave velocities of 2480 ms^{-1} for the delay-line and 1006 ms^{-1} for the rubber, both measured experimentally. Once the tire/WAAM interface was identified via the SAFT algorithm, the ToF's through the three mediums were computed to construct the adaptive TFM images with the additional longitudinal velocity of the titanium (6100 ms^{-1}). The velocity values were found without significant variations after the measurements in pulse-echo mode using single element transducers.

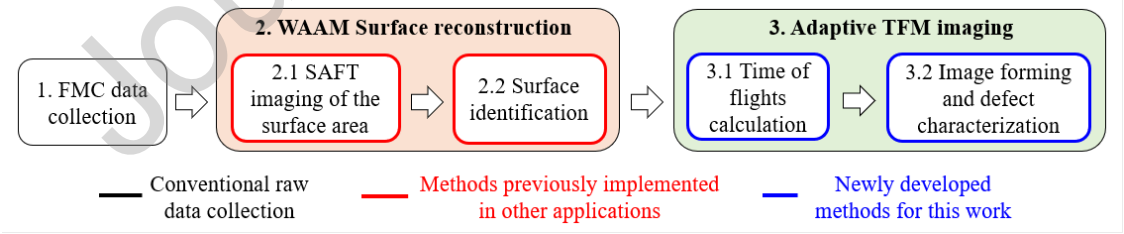

Figure 8 Diagram illustrating the SAFT surface finding and TFM imaging processing of the collected FMC data

5 Automated Dry-Coupled In-Situ Ultrasonic Inspection of As-Built Titanium WAAM Components

5.1 Titanium WAAM Verification Wall with Artificially Drilled Reflectors

An initial experiment was conducted on a Ti-64 test specimen manufactured using the plasma arc WAAM process and oscillation deposition strategy. Five layers with an approximate height of 2.5 mm per layer and a width of 35 mm were deposited on a 12 mm thick base plate. Two artificial defects were fabricated in the form of Bottom-drilled Holes (BH) with diameters of 1 mm and 2 mm respectively and extending up by 14 mm into the sample, as shown in Figure 9.

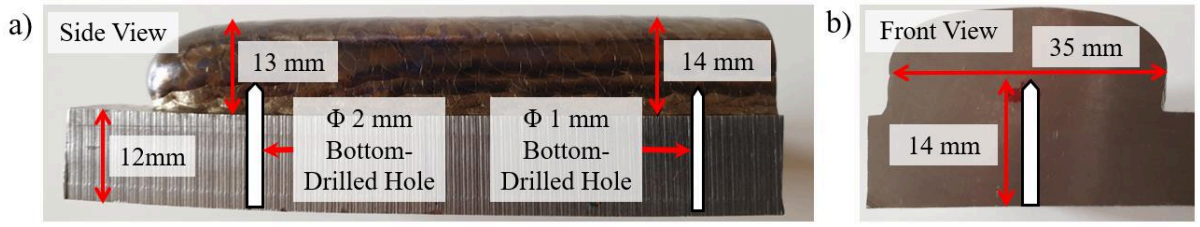

Figure 9 (a) Side view and (b) front view of a WAAM Ti-64 component deposited using oscillation strategy and containing fabricated calibration bottom-drilled holes of 1 mm and 2 mm in diameter

5.1.2 Titanium WAAM Verification Wall Surface Reconstruction

The FMC dataset corresponding to the sample with 2 mm BH was processed and analyzed for the WAAM surface profile estimation. For the SAFT processes used in this paper, the images were calculated using an angle limitation α = -7.5° and β=7.5° which was found to be the most accurate during initial trials and the image dB scale set to 0 to -30 to best visualize individual features of the image without noise disturbance.

A clear representation of the contour of the WAAM surface (dashed green box) can be observed on the SAFT image in Figure 10 (a). Furthermore, a strong signal indicating the end of the coupling area between the roller-probe's tire and the WAAM surface (*i.e.,* decoupling points) are also visible and marked (dashed red box). Below the surface contour in the image, the repeated signal of the tire/sample interface can also be seen (dashed yellow box).

Prior to deploying the WAAM surface finding, it was necessary to separate the signal of the WAAM contour from the signal received for decoupling points. The coupled width of the tire/WAAM interface was found to be 30 mm, obtained from measuring the distance between the decoupling points and used to determine the maximum width over which the curve fitting was performed.

Signal amplitudes lower than -10 dB of the maximum image amplitude were then filtered to discard any noise from the image. Owing to the thresholding, the image pixels with the highest signal amplitudes were successfully identified and a curve fitted through them to represent the WAAM surface, as shown in Figure 10 (b). The SAFT surface finding performance was evaluated by comparing the reconstructed surface against surface profiles obtained via a non-contact metrology laser scan with a y-axis resolution of 12 µm [58] (Figure 10 (c)). The total number of points along the x-axis for the profile acquired by the laser was 300 resulting in a spatial sampling of 0.1 mm. To quantify the discrepancy between the two curves, the average error between the two profiles was calculated through:

$$\Delta_{average} = \frac{1}{k}\sum_{k=1}^{k=n} |Y_{True}^{k} - Y_{UT}^{k}| \quad (8)$$

where n is the total number of points used in the curve fitting (n = 300), k is the point number along the x-axis of both the true surface profile and the SAFT estimated surface profile, and Y stands for the y-axis position of points. The calculation was only performed within an interval where both surfaces exist. The average error between the profiles (visualized in Figure 10 (d)) was calculated using Equation 8 as 0.06 mm. It is worth noting, that given the phased array sampling frequency of 50 MHz and the longitudinal wave velocity of Ti-64 (velocity = 6100 ms^{-1}) results in a distance resolution of a minimum 0.12 mm within the Ti-64 medium; double the developed SAFT surface reconstruction algorithm resolution.

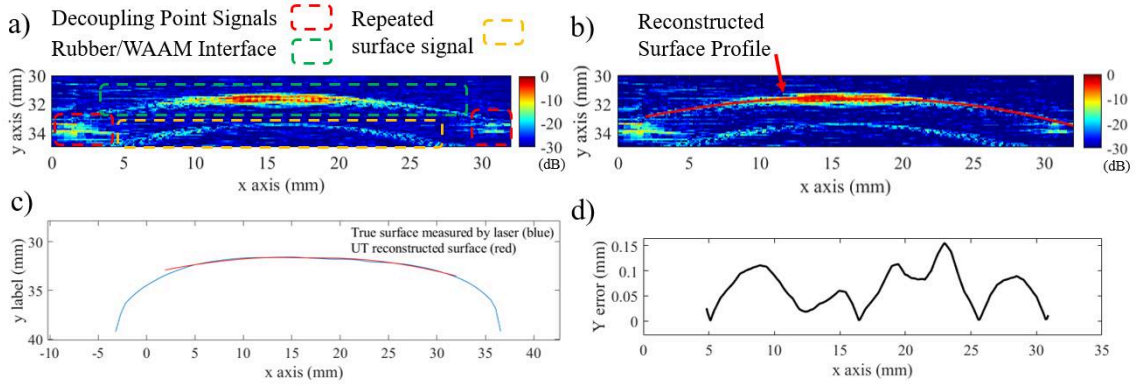

Figure 10 (a) An image of the WAAM surface formed using the dual-medium SAFT algorithm, (b) fitted curve to the extracted high-intensity surface points of the SAFT image after filtering and denoising, (c) comparison between the laser-scanned surface profile and the SAFT reconstructed profile, and (d) measured error between the surface profile acquired by laser and through SAFT reconstruction of the Ti-64 WAAM with bottom-drilled holes

5.1.3 Titanium WAAM Verification Wall TFM Image Reconstruction

Figure 11 depicts the results of the TFM imaging for the two BHs in the Ti-64 WAAM sample, after incorporating the reconstructed WAAM surface profile estimated in Section 5.1.2. This figure displays the two imaged sections of the WAAM component located immediately beneath the roller-probe and the two BHs. The TFM images reconstructed from this data are shown in the green box in Figures 11 (a) and (b) for BHs of 2 mm and 1 mm, respectively. As demonstrated in the figure, both the 1 mm and 2 mm defects were successfully detected and their indications evident in the reconstructed TFM images. To facilitate the detectability, the area in the immediate vicinity of the defect was windowed to exclude the surface signal and its trailing noise from the computation.

In order to size the defects, a horizontal line parallel to the *x*-axis and passing through the pixel with the highest defect signal was selected in each of the TFM images, and the pixel values along this line were plotted in Figure 12. The analysis was carried out using the 6-dB drop technique, recognized as a conventional flaw sizing methodology in ultrasound inspections [59]. This was achieved by superimposing a horizontal line through the intensity plots at a level where the amplitude reduces by 6dB from the maximum signal amplitude of the defect and measuring the distance between the intersection points. The lengths measured were 1.3mm and 1.88 mm for 1mm and 2mm defect, respectively.

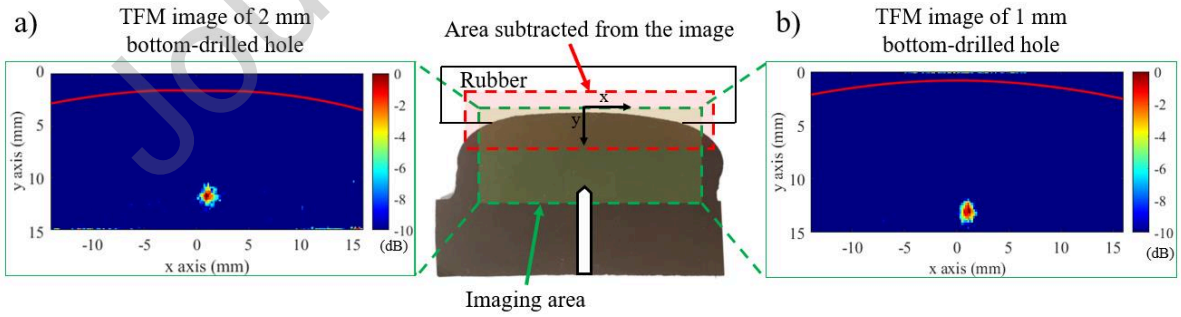

Figure 11 TFM image reconstructions for bottom-drilled holes of: (a) 2 mm, and (b) 1 mm in diameter inside a Ti-64 WAAM component

For the images of Figure 12, SNR was calculated to assess the overall image quality and detection capability of the inspection configuration. To this end, the root mean square of the noise data presented in the plots of Figure 12, excluding the signal of the defect, was calculated to indicate the noise level. Subsequently, the SNR was obtained as the ratio of the maximum defect amplitude to the average noise level. It can be observed from the results of Figures 11 and 12 that an SNR of at least 15 dB was achieved for the smallest defect.

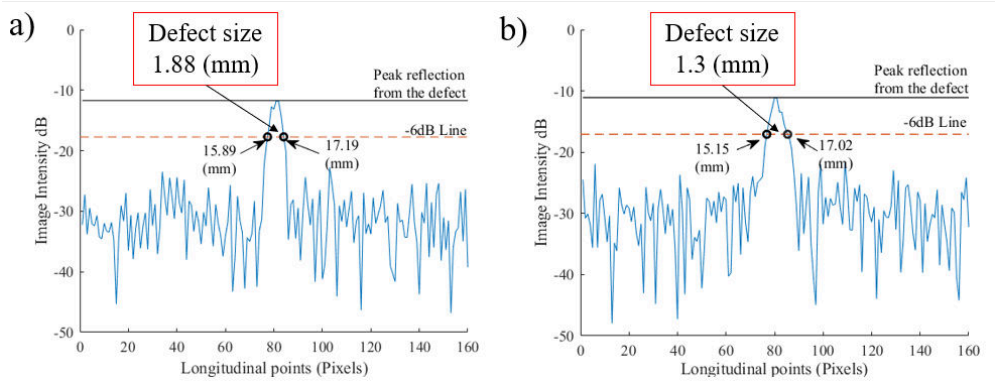

Figure 12 Pixel intensity values plotted alongside horizontal lines at -6 dB of the maximum image amplitudes passing through the maximum signals of a) 2 mm and b) 1 mm defects to size defects indications

5.2.1 Titanium WAAM with Artificially Induced LoF Defects

After successful verification on the above sample with artificial defects, experiments were also carried out on a Ti-64 WAAM wall (Figure 13), deposited with an oscillation strategy containing intentionally induced defects. The component (45 x 25 x 300 mm (H x W x L)) had intentional LoF defects introduced during the process at layer 6, located 30 mm above the baseplate, by decreasing the arc current from 100% to 70% and increasing the travel speed from 100% to 125%. For the next layer, the welding current was restored to 100% again, but the travel and the wire feeding speeds were reduced from 100% to 70% to repair the morphology of the previous layer. This process was used to smoothen the discontinuities generated within the previous layer and to maintain the final shape of the component, however, despite the repair process, some LoF defects were expected to remain in the component. To verify the existence of these defects, reference XCT tests were conducted using a Nikon XT H 225/320 LC X-ray computer tomography system fitted with a 225kV X-ray source. A maximum resolution of 100 µm was achieved, given the dimensions of the Ti-64 component, its placement within the XCT chamber, and its distance from the X-ray source. The wall was then inspected using the PAUT roller-probe and FMC data collected to compare with the XCT data.

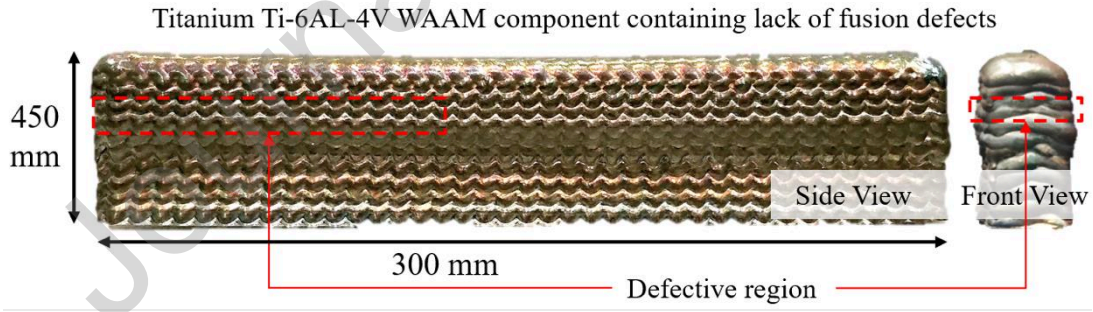

Figure 13 Ti-64 WAAM specimen deposited by oscillation strategy and containing process-induced intentional deposition lack of fusion defects spread over the marked area

5.2.2 Titanium WAAM with Artificially Induced LoF Defects Surface Reconstruction

The FMC dataset acquired was also analyzed using the SAFT algorithm to estimate the surface contour and the results presented in Figure 14. A strong indication of the WAAM surface, as well as reflections of the decoupling points, were clearly distinguishable (Figure 14 (a)). Following the same procedure described in Section 5.1.2 for the SAFT images, the width of the contact area was determined (15 mm), the image filtered for amplitudes lower than -10 dB of the maximum and a 4th order polynomial fitted to the high-intensity surface points as depicted in Figure 14 (b).

Again, the SAFT surface finding performance was evaluated by comparing the reconstructed surface against surface profiles obtained via a non-contact metrology laser scan [58] and the average surface estimation error, presented in Figure 14 (d), was calculated to be 0.04 mm. Moreover, it can be seen in Figure 14 (d) that a lower surface mismatch was observed at the center of the two profiles where the tire was fully coupled to the

peak of the WAAM surface. This may suggest better performance of the algorithm for the surface points closer to the center of the array. Although the error value continued to grow towards the corners of the WAAM, reaching up to 0.09 mm, it was still smaller than the ultrasonic spatial resolution permissible at the fixed sampling frequency.

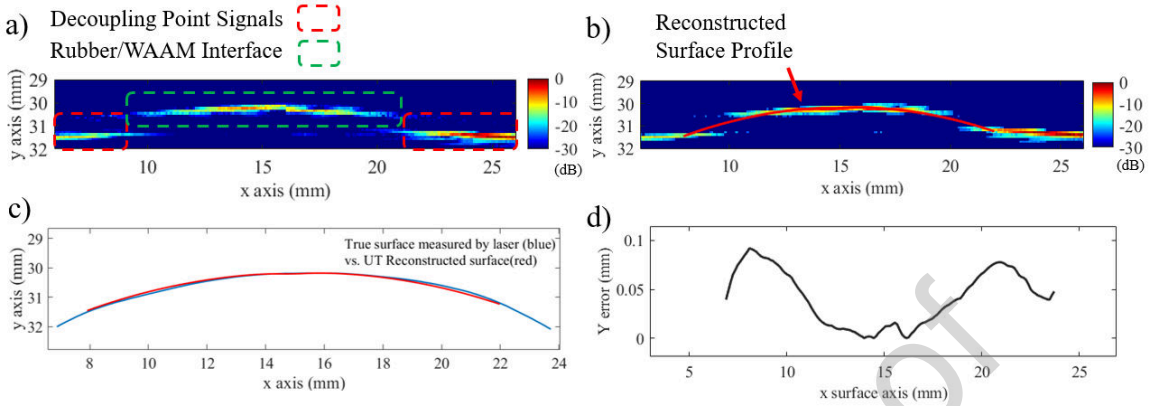

Figure 14 (a) An image of the WAAM surface formed using the dual-medium SAFT algorithm, (b) fitted curve to the extracted high-intensity surface points of the SAFT image after filtering and denoising, (c) comparison between the laser-scanned surface profile and the SAFT reconstructed profile, and (d) measured error between the surface profile acquired by laser and through SAFT reconstruction of the Ti-64 WAAM with intentional defects

5.2.3 Titanium WAAM with Artificially Induced LoF Defects TFM Image Reconstruction

Figure 15 (a) shows three inspection positions, correspondingly aligned to the areas with induced process-driven defects and which possessed the highest signal amplitude in the acquired ultrasonic data stream. The surface profiles were calculated at these points and the TFM images were computed for a rectangular area of 10 mm by 20 mm across the *y* and *x*-axes, respectively. The images were normalized by the maximum signal amplitude and plotted on a 10 dB scale in Figure 15.

Figures 15 (b), (c), and (d) show that the ultrasonic indications of the three LoF defects, located at different positions in the Ti-64 WAAM were readily detectable in the resultant TFM images. For the reference XCT images, a full 3D model of the WAAM component was reconstructed, the model sliced at the corresponding TFM image location along the z-axis, and a 2D grayscale representation of the defect was processed. The TFM results were then compared with those obtained from the XCT analysis in the same location. To aid readability, the TFM images corresponding to each of the defects on the XCT frames are presented in a green rectangular window beside their XCT counterpart. The dimensions of the targeted defects were measured from the XCT images to be approximately 0.5 x 6 x 0.5 mm (H x W x L). It is The SNR of the images was measured to be a minimum of 10 dB which is deemed acceptable, given the coupling method, surface waviness and attenuation within the roller-probe's tire. Moreover, it is worth mentioning that the defects themselves are not pure cavities but fragmented, varying in shape and thus, signal retrieved must therefore be considered adequate. In terms of defect locations, good agreement was found between the depth and the horizontal position of the defects measured from the TFM images and those from the XCT images.

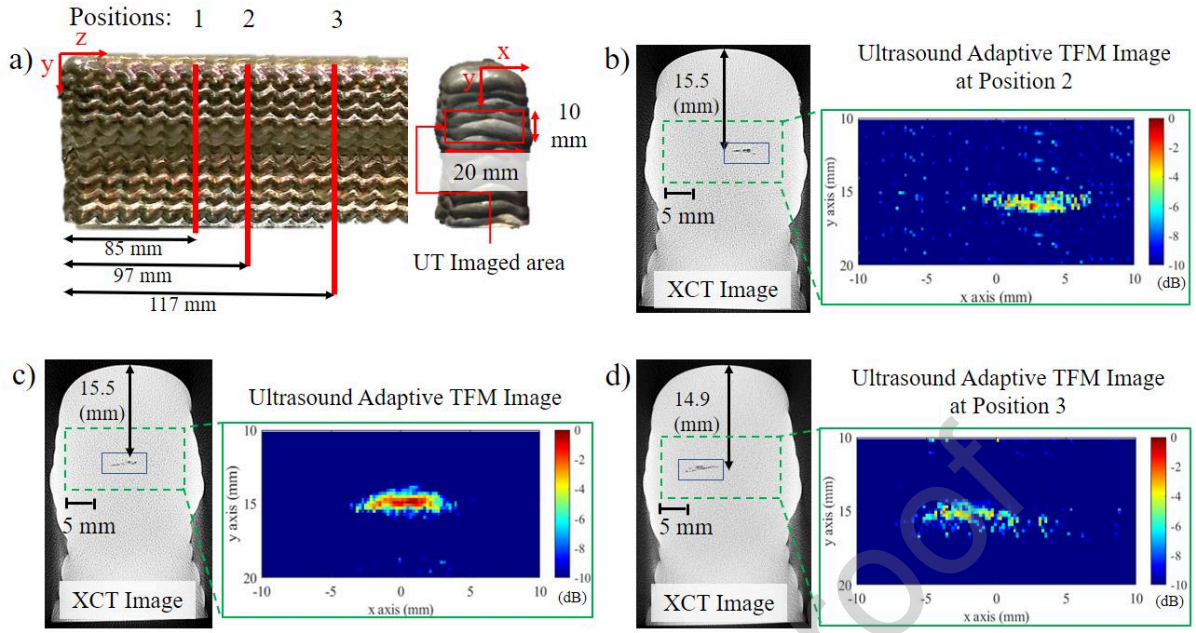

Figure 15 (a) Roller-probe Ti-64 WAAM inspection positions where FMC data sets were collected, and a comparison between the results of adaptive TFM imaging and those obtained by XCT tests for the defects at positions (b) 1, (c) 2, and (d) 3

5.2.4 Automated As-Built WAAM Component Ultrasonic Volumetric Coverage Considerations

One further advantage of the DAS TFM algorithm proposed in this study can be summarised by referring to the raytracing diagram presented for the last element of the array in Figure 16. As the Figure suggests, even the waves generated by the array elements located at the extremities of the active aperture have significant contributions to the final TFM image. This is particularly interesting when tracing the ray from element 64 to the lateral pixels (Figure 16(a)) and bottom pixels located 40 mm inside the sample (Figure 16 (b)), showing that the refraction angles across the interfaces allow for the rays to reach these image points. This observation emphasizes that despite the very small contact area between the rubber tire and WAAM surface, the natural as-built component surface convexity works in the favour of the raytracing approach allowing for the WAAM internal structure to be accessible by the ultrasound energy, even if it is generated by the corner elements. One distinct advantage of this technique is in that it allows imaging a wider area than the coupled surface without the need to reduce the number of contributing n^2 elements and therefore utilizing the whole FMC dataset. The high acoustic mismatch between the tire rubber (1.12 MRayls) and Ti-64 WAAM (27.49 MRayls) components leads to high refraction angles; therefore, redirecting the sound wave towards the corners of the test piece. However, it should be noted that the large acoustic mismatch also negatively impacts the signal amplitude transmitted into the component by increasing the reflected wave energy at the interface of the rubber tire and WAAM surface.

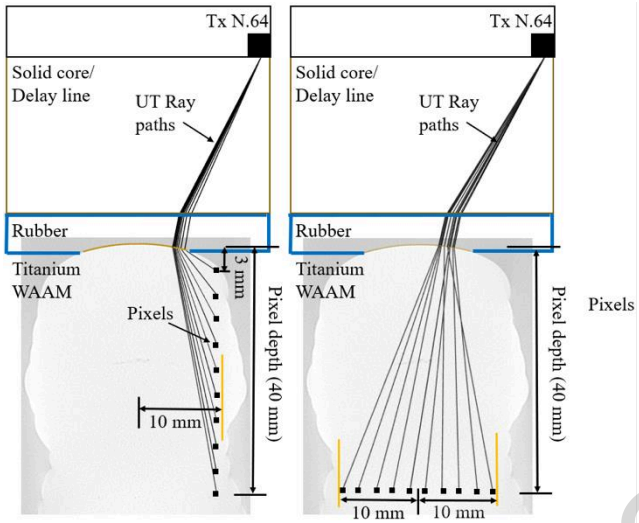

Figure 16 Ray tracing from corner element number 64 to the TFM image (a) lateral pixels extending from 3 mm to 40 mm below the WAAM surface, and (b) bottom pixels at the depth of 40 mm spread across the width of the Ti-64 WAAM component

6 Conclusions

6.1 Conclusion

This work presented, for the first time, the concept of a three-layer adaptive ultrasound TFM imaging algorithm for the inspection of WAAM components from their non-planar as-built surface, eliminating the necessity for a post-manufacturing surface milling. An integrated SAFT-based approach reconstructs the as-built surface and interface when deploying a customized ultrasound roller-probe. The functionality and performance of the concept approach were demonstrated on two different Ti-64 WAAM components, one with bottom drilled holes of 2 mm and 1 mm in the diameter and the other containing intentionally induced LoF defects as small as 0.5 x 5 x 0.5 mm (H x W x L). The following summarizes the findings and the conclusions of this manuscript:

- Using acquired FMC data, the as-built non-planar tire/WAAM interface was reconstructed using the SAFT algorithm. Distinctive surface profiles emerging on the SAFT images allowed for the integration of an automated surface finding algorithm, based on curve fitting, allowing suitable reconstruction of the WAAM surface curvature.
- The SAFT reconstruction of the as-built WAAM component was evaluated against a reference scan obtained via a non-contact metrology laser scan and the average relative error calculated as 0.04 mm.
- The ultrasonic measurement of the non-planar as-built surface geometry of the WAAM components and the time of flights of the ultrasonic rays traversing between the array and every pixel of the image was computed accommodating refractions at the two interfaces of the delay-line/rubber tire and rubber tire /WAAM sample.
- Despite the restricted contact area of only 15 mm between the rubber tire and the WAAM surface, the ray-tracing algorithm demonstrated that when using the roller-probe on WAAM walls provides thorough coverage of the interior volume, even when the wave is generated by corner elements.
- A fully focused image of Ti-64 WAAM components was computed and formed using the adaptive TFM algorithm with BHs and LoF defects induced at selected locations inside the WAAM components detected and imaged with SNR greater than 10dB.
- The formed TFM images of the induced LoF defects were compared to reference XCT results where strong agreement between the results was observed in terms of the defect location and extension, confirming the competency of the novel imaging approach.

The proposed new inspection concept and the methodology provides a new inspection alternative to imaging of as-built WAAM components, removing the need for costly surface machining operations. The proposed methodology easily conforms to the complexities of the non-planar as-built WAAM surface and accommodates surface profile curvature in image calculations with a high degree of accuracy. The approach unlocks the poten-

tial for ultrasonic phased array volumetric, or in-process multi-layer-specific, an inspection of WAAM components without the need for subsequent post-processing or machining.

6.2 Future Work

Future activities are to be centered around improving PAUT transduction, automated probe deployment during the WAAM build process, taking advantage of a dwell time between layers, that can allow up to minutes for inspection to be performed [60]. Alternatively, further, utilize the advantage of the high-temperature roller-probe and investigate the deployment while the torch is depositing elsewhere.

For the in-situ deployment, the key aim is to investigate the effect of the temperature gradients within the deposited component on ultrasonic wave propagation (velocity, refraction, and attenuation) along with the subsequent development of adaptive compensation algorithms. The velocity calibration and compensation for the anisotropic materials is to be developed, allowing for precise ray tracing within the components.

Lastly, the authors aim to investigate a comprehensive Probability of Detection (PoD) study focused on defect detectability and sizing in deposited WAAM components. Additionally, realizing the importance of deployment within the actual WAAM build process, the PAUT probe and imaging algorithms will be further optimized for automated deployment and acquisition during the WAAM deposition process at speed.

Author Statement

Rastislav Zimermann Conceptualization, Software, Validation, Formal analysis, Investigation, Writing – Original Draft, . Ehsan Mohseni Conceptualization, Software, Validation, Formal analysis, Investigation, Writing – Review & Editing, Visualisation, Investigation. David Lines. Conceptualization, Validation, Writing – Review & Editing. Randika K. W. Vithanage. Conceptualization, Validation, Writing – Review & Editing. Charles N. Macleod. Conceptualization, Resources, Supervision, Project administration, Funding acquisition, Review & Editing. Stephen G. Pierce. Supervision, Project administration, Funding acquisition, Review & Editing. Anthony Gachagan Supervision, Project administration, Funding acquisition, Review &. Editing. Yashar Javadi. Conceptualization, Writing – Review & Editing. Stewart WilliamsSupervision, Project administration, Funding acquisition, Review & Editing. Jialou Ding. Supervision, Project administration, Funding acquisition, Review & Editing

Declaration of interests

☒ The authors declare that they have no known competing financial interests or personal relationships that could have appeared to influence the work reported in this paper.

☐The authors declare the following financial interests/personal relationships which may be considered as potential competing interests:

Acknowledgements

The project was supported by (I) NEWAM (EP/R027218/1), (II) EPSRC Doctoral Training Partnership (DTP) (EP/R513349/1) and (III) RoboWAAM (EP/P030165/1). We would like to thank Dr Alice Macente, for the XCT data acquisition and reconstruction, and the Scottish Funding Council's Oil and Gas Innovation Centre for funding the X-ray Computed Tomography scanner at the University of Strathclyde, owned by the Civil & Environmental Engineering

References

1. Standardization, I.O.f., *Additive Manufacturing: General: Principles: Terminology*. 2015: ISO.
2. Paolini, A., S. Kollmannsberger, and E. Rank, *Additive manufacturing in construction: a review on processes, applications, and digital planning methods, Addit. Manuf. 30 (2019) 100894*. 2019.
3. Herzog, D., et al., *Additive manufacturing of metals.* Acta Materialia, 2016. **117**: p. 371-392.
4. Williams, S.W., et al., *Wire+ arc additive manufacturing.* Materials Science and Technology, 2016. **32**(7): p. 641-647.
5. Martina, F., et al., *Investigation of the benefits of plasma deposition for the additive layer manufacture of Ti–6Al–4V.* Journal of Materials Processing Technology, 2012. **212**(6): p. 1377-1386.
6. Banerjee, D. and J. Williams, *Perspectives on titanium science and technology.* Acta Materialia, 2013. **61**(3): p. 844-879.
7. Colegrove, P., et al. *System architectures for large scale wire+ arc Additive Manufacture*. in *10th International Conference on Trends in Welding Research*. 2016.
8. Xu, X., et al., *Preliminary investigation of building strategies of maraging steel bulk material using wire+ arc additive manufacture.* Journal of Materials Engineering and Performance, 2019. **28**(2): p. 594-600.
9. Xu, X., et al., *Oxide accumulation effects on wire+ arc layer-by-layer additive manufacture process.* Journal of Materials Processing Technology, 2018. **252**: p. 739-750.
10. Wu, B., et al., *A review of the wire arc additive manufacturing of metals: properties, defects and quality improvement.* Journal of Manufacturing Processes, 2018. **35**: p. 127-139.
11. Lopez, A., et al., *Non-destructive testing application of radiography and ultrasound for wire and arc additive manufacturing.* Additive Manufacturing, 2018. **21**: p. 298-306.
12. LEVCUN, G.A. and C.S. MAHENDRA, *Computed Radiography in the Pacific Northwest: Benefits, Drawbacks, and Requirements.* AMMTIAC Quarterly, 2007: p. 11-14.
13. Kourra, N., et al., *Computed tomography metrological examination of additive manufactured acetabular hip prosthesis cups.* Additive Manufacturing, 2018. **22**: p. 146-152.
14. Mireles, J., et al., *Analysis and correction of defects within parts fabricated using powder bed fusion technology.* Surface Topography: Metrology and Properties, 2015. **3**(3): p. 034002.
15. Naito, S., S. Yamamoto, and S. Yamamoto. *Novel X-ray backscatter technique for detecting crack below deposit*. in *7th International Conference on NDE in Relation to Structural Integrity for Nuclear and Pressurized Components*. 2010.
16. García-Martín, J., J. Gómez-Gil, and E. Vázquez-Sánchez, *Non-destructive techniques based on eddy current testing.* Sensors, 2011. **11**(3): p. 2525-2565.
17. Bento, J.B., et al., *Non-destructive testing for wire+ arc additive manufacturing of aluminium parts.* Additive Manufacturing, 2019. **29**: p. 100782.
18. Zhang, J., et al., *Crack path selection at the interface of wrought and wire+ arc additive manufactured Ti–6Al–4V.* Materials & Design, 2016. **104**: p. 365-375.

19. Du, W., et al., *Eddy current detection of subsurface defects for additive/subtractive hybrid manufacturing.* The International Journal of Advanced Manufacturing Technology, 2018. **95**(9): p. 3185-3195.
20. Lopez, A., et al. *Mapping of non-destructive techniques for inspection of wire and arc additive manufacturing*. in *Proceedings of the 7th International Conference on Mechanics and Materials in Design, Portugal*. 2017.
21. Javadi, Y., et al. *Intentional weld defect process: from manufacturing by robotic welding machine to inspection using TFM phased array*. in *AIP Conference Proceedings*. 2019. AIP Publishing LLC.
22. Willcox, M. and G. Downes, *A brief description of NDT techniques.* Toronto: NDT Equipment Limited, 2003.
23. Javadi, Y., et al., *In-process inspection of multi-pass robotic welding.* Review of Progress in Quantitative Nondestructive Evaluation, 2019.
24. Javadi, Y., et al., *Continuous monitoring of an intentionally-manufactured crack using an automated welding and in-process inspection system.* Materials & Design, 2020: p. 108655.
25. Pieris, D., et al., *Laser Induced Phased Arrays (LIPA) to detect nested features in additively manufactured components.* Materials & Design, 2020. **187**: p. 108412.
26. Zeng, Y., et al., *Laser Ultrasonic inspection of a Wire+ Arc Additive Manufactured (WAAM) sample with artificial defects.* Ultrasonics, 2020: p. 106273.
27. Bakre, C., M. Hassanian, and C. Lissenden. *Influence of surface roughness from additive manufacturing on laser ultrasonics measurements*. in *AIP Conference Proceedings*. 2019. AIP Publishing LLC.
28. Chimenti, D., *Review of air-coupled ultrasonic materials characterization.* Ultrasonics, 2014. **54**(7): p. 1804-1816.
29. Javadi, Y., et al., *Ultrasonic phased array inspection of a Wire+ Arc Additive Manufactured (WAAM) sample with intentionally embedded defects.* Additive Manufacturing, 2019. **29**: p. 100806.
30. Lopez, A.B., et al., *Phased Array Ultrasonic Inspection of Metal Additive Manufacturing Parts.* Journal of Nondestructive Evaluation, 2019. **38**(3): p. 62.
31. Mohseni, E., et al. *Ultrasonic phased array inspection of wire plus arc additive manufactured (WAAM) titanium samples*. in *58th Annual British Conference on Non-Destructive Testing*. 2019.
32. Chabot, A., et al., *Towards defect monitoring for metallic additive manufacturing components using phased array ultrasonic testing.* Journal of Intelligent Manufacturing, 2019: p. 1-11.
33. Chauveau, D., *Review of NDT and process monitoring techniques usable to produce high-quality parts by welding or additive manufacturing.* Welding in the World, 2018. **62**(5): p. 1097-1118.
34. Knezović, N. and B. Dolšak, *In-process non-destructive ultrasonic testing application during wire plus arc additive manufacturing.* Advances in Production Engineering & Management, 2018. **13**(2): p. 158-168.
35. Xiong, X., H. Zhang, and G. Wang, *Metal direct prototyping by using hybrid plasma deposition and milling.* Journal of Materials Processing Technology, 2009. **209**(1): p. 124-130.
36. Lockett, H., et al., *Design for Wire+ Arc Additive Manufacture: design rules and build orientation selection.* Journal of Engineering Design, 2017. **28**(7-9): p. 568-598.
37. Olympus-ims.com. *Ultrasonic phased array wedge for inspecting high-temperature parts up to 150°C*. 2020 [cited 2020 16/11/2020]; Available from: https://www.olympus-ims.com/en/applications/ultrasonic-phased-array-wedge-for-inspecting-high-temperature-parts-up-to-150c/#:~:text=As%20phased%20array%20probes%20heat,temperature%20of%2060%20%C2%B0C.
38. Hagglund, F., et al. *A novel phased array ultrasonic testing (PAUT) system for on-site inspection of welded joints in plastic pipes*. in *Proceedings of the 11th European Conference on Non-Destructive Testing (ECNDT), Prague, Czech Republic*. 2014.

39. Stratoudaki, T., et al. *Laser induced phased arrays for remote ultrasonic imaging of additive manufactured components*. in *57th Annual Conference of the British Institute of Non-Destructive Testing, NDT 2018*. 2018.
40. Lines, D., et al. *Using coded excitation to maintain signal to noise for FMC+ TFM on attenuating materials*. in *2019 IEEE International Ultrasonics Symposium (IUS)*. 2019. IEEE.
41. Drinkwater, B., R. Dwyer-Joyce, and P. Cawley, *A study of the transmission of ultrasound across solid–rubber interfaces.* The Journal of the Acoustical Society of America, 1997. **101**(2): p. 970-981.
42. Vithanage, R.K., et al., *A phased array ultrasound roller probe for automated in-process/interpass inspection of multipass welds.* IEEE Transactions on Industrial Electronics, 2020.
43. Drinkwater, B. and P. Cawley, *AN ULTRASONIC WHEEL PROBE AL TERNA TIVE TO LIQUID COUPLING.* 1994.
44. Mineo, C., et al. *Flexible integration of robotics, ultrasonics and metrology for the inspection of aerospace components*. in *AIP conference proceedings*. 2017. AIP Publishing LLC.
45. Mineo, C., et al. *Fast ultrasonic phased array inspection of complex geometries delivered through robotic manipulators and high speed data acquisition instrumentation*. in *2016 IEEE International Ultrasonics Symposium (IUS)*. 2016. IEEE.
46. Mohseni, E., et al. *A high temperature phased array ultrasonic roller probe designed for dry-coupled in-process inspection of wire+ arc additive manufacturing*. in *47th Annual Review of Progress in Quantitative Nondestructive Evaluation*. 2020.
47. Zhang, J., B.W. Drinkwater, and P.D. Wilcox, *Efficient immersion imaging of components with nonplanar surfaces.* IEEE transactions on ultrasonics, ferroelectrics, and frequency control, 2014. **61**(8): p. 1284-1295.
48. Holmes, C., B.W. Drinkwater, and P.D. Wilcox, *Post-processing of the full matrix of ultrasonic transmit–receive array data for non-destructive evaluation.* NDT & e International, 2005. **38**(8): p. 701-711.
49. Fan, C. and B.W. Drinkwater. *Comparison between beamforming and super resolution imaging algorithms for non-destructive evaluation*. in *AIP Conference Proceedings*. 2014. American Institute of Physics.
50. Holmes, C., B. Drinkwater, and P. Wilcox, *The post-processing of ultrasonic array data using the total focusing method.* Insight-Non-Destructive Testing and Condition Monitoring, 2004. **46**(11): p. 677-680.
51. Han, X.-l., et al. *Application of ultrasonic phased array total focusing method in weld inspection using an inclined wedge*. in *Proceedings of the 2014 Symposium on Piezoelectricity, Acoustic Waves, and Device Applications*. 2014. IEEE.
52. Le Jeune, L., et al. *Adaptive ultrasonic imaging with the total focusing method for inspection of complex components immersed in water*. in *AIP Conference proceedings*. 2015. American Institute of Physics.
53. Kerr, W., S. Pierce, and P. Rowe, *Investigation of synthetic aperture methods in ultrasound surface imaging using elementary surface types.* Ultrasonics, 2016. **72**: p. 165-176.
54. Malkin, R.E., et al., *Surface reconstruction accuracy using ultrasonic arrays: Application to non-destructive testing.* NDT & E International, 2018. **96**: p. 26-34.
55. Nicolas Badeau, G.P.-A., Alain Le Duff. *Use of the Total Focusing Method with the Envelope Feature*. 30 March 2020 [accessed 9 April 2020]; Available from: https://www.olympus-ims.com/en/resources/white-papers/use-of-the-total-focusing-method-with-the-envelope-feature/.
56. Parrilla, M., et al. *Dynamic focusing through arbitrary geometry interfaces*. in *2008 IEEE Ultrasonics Symposium*. 2008. IEEE.
57. Vithanage, R.K.W., et al., *A phased array ultrasound roller probe for automated in-process/interpass inspection of multipass welds.* IEEE Transactions on Industrial Electronics, 2020: p. 1-1.
58. *Compact laser scanner for automation & robotics*. 2021 [cited 2021 11/02]; Available from: https://www.micro-epsilon.co.uk/2D_3D/laser-scanner/scanCONTROL-2600/.

59. Ciorau, P., J. Coulas, and T. Armitt, *A contribution to length sizing of weld flaws using conventional, PAUT and TOFD ultrasonic techniques.* NDT. net, 2011(11).
60. Vázquez, L., et al., *Influence of interpass cooling conditions on microstructure and tensile properties of Ti-6Al-4V parts manufactured by WAAM.* Welding in the World, 2020. **64**: p. 1377-1388.

Highlights

- Multi-Layer Adaptive TFM for Roller-Probe inspection of AM components
- Roller-Probe surface reconstruction of Additive Manufacture components
- Inspection of as-built Titanium WAAM components with artificial and actual defects

Multi-layer ultrasonic imaging of as-built wire + arc additive manufactured components

Zimermann, Rastislav

2021-10-13

Zimermann R, Mohseni E, Lines D, et al., (2021) Multi-layer ultrasonic imaging of as-built wire + arc additive manufactured components. Additive Manufacturing, Volume 48, Part A, December 2021, Article number 102398

https://doi.org/10.1016/j.addma.2021.102398